Inhomogeneous *d*-wave superconducting state of a doped Mott insulator

Ziqiang Wang, Jan R. Engelbrecht, Shancai Wang, and Hong Ding
Department of Physics, Boston College, Chestnut Hill, Massachusetts 02467

Shuheng H. Pan
Department of Physics, Boston University, Boston, Massachusetts 02215

Recent atomic resolution scanning tunneling microscope (STM) measurements discovered remarkable electronic inhomogeneity, i.e., nanoscale spatial variations of the local density of states (LDOS) and the superconducting energy gap, in the high-T_c superconductor $Bi_2Sr_2CaCu_2O_{8+x}$. Based on the experimental findings, we conjectured that the inhomogeneity arises from variations in local oxygen doping level and may be generic of doped Mott insulators. In this paper, we provide theoretical support for this picture. We study a doped Mott insulator within a generalized t-J model, where doping is accompanied by ionic Coulomb potentials centered in the BiO plane located a distance d_s away from the CuO_2 plane. We solve, at the mean-field level, a set of spatially unrestricted Bogoliubov–de Gennes equations self-consistently to obtain the distributions of the hole concentration, the valence bond, and the pairing order parameters for different nominal/average doping concentrations. We calculate the LDOS spectrum, the integrated LDOS, and the local superconducting gap as those measured by STM, make detailed comparisons to experiments, and find remarkable agreement with the experimental data. We emphasize the unconventional screening of the ionic potential in a doped Mott insulator and show that nonlinear screening dominates on nanometer scales, comparable to the short coherence length of the superconductor, which is the origin of the electronic inhomogeneity. It leads to strong inhomogeneous redistribution of the local hole density and promotes the notion of *local doping concentration* (LDC). We find that the inhomogeneity structure manifests itself at all energy scales in the STM tunneling differential conductance, and elucidate the similarity and the differences between the data obtained in the constant tunneling current mode and the same data normalized to reflect constant tip-to-sample distance. We also discuss the underdoped case where nonlinear screening of the ionic potential turns the spatial electronic structure into a percolative mixture of patches with smaller pairing gaps embedded in a background with larger gaps to single particle excitations.

I. INTRODUCTION

The parent compounds of the high-T_c superconductors are stoichiometric Mott insulators.[1] In principle, carriers can be introduced into the insulating state either by field effect or by chemical doping, but to date high-T_c superconductivity in the cuprates has only been found to arise when they are properly doped away from stoichiometry. In the case of $YBa_2Cu_3O_{7-x}$ (YBCO) and $Bi_2Sr_2CaCu_2O_{8+x}$ (BSCCO), the dopants are the excess oxygen atoms. The latter inject holes into the CuO_2 planes, leaving behind the negatively charged oxygen ions. While for YBCO, the dopant ions go into the copper oxide chains and can be arranged more periodically,[2] in the case of BSCCO, the dopants, with a concentration of x, disorder themselves in the semiconducting BiO layer which is about 5 Å away from the CuO_2 plane where superconductivity is believed to originate.

In addition to doping holes into the CuO_2 planes, the dopant oxygen atoms inevitably introduce long-range random ionic potentials that scatter the carriers in the copper-oxide plane in analogy to the situation encountered in two-dimensional (2D) electron systems in modulation doped semiconductors. This has the potential to cause the electronic structure in the copper-oxide plane to be inhomogeneous. Early neutron scattering,[3] tunneling,[4] and STM[5] data showed features that could be accounted for by inhomogeneity, but

they were usually attributed to sample quality. The common view, which is largely based on the physics of ordinary metals, has been that the ionic potential in a high-quality crystal would be screened by phonons and by the carriers in the plane such that charges distribute uniformly and are accommodated by a homogeneous electronic structure; albeit that the latter has the tendency toward microscopic phase separation[6] due to strong electronic correlations. This viewpoint appears to be supported, to a certain extent, by transport[7] and photoemission[8] measurements on BSCCO which observe quasiparticles with relatively well-defined momentum, a mean-free path of about 100 Å in the nodal direction, and a transport mean-free path of about 400 Å.

However, this conventional view has been seriously challenged by recent low-temperature STM measurements on BSCCO.[9–11] In Ref. 9, Pan *et al.* (hereafter referred to as "we") observed spatially cross-correlated variations in the LDOS and the superconducting energy gap on a remarkably short length scale of about 14 Å. We identified this as the gap amplitude coherence length or the pair size. It directly confirms the local pairing nature in the high-T_c superconductor. The magnitude of the superconducting gap has a Gaussian distribution with a mean value of 42 meV, close to the gap value obtained from planar tunneling,[12] and a full-width-half-maximum of about 20 meV. This variance coincides with the intrinsic width ($\sim$20 meV) of the coherence peak

measured by angle resolved photoemission spectroscopic (ARPES) near the antinodes where the d-wave gap is at its maximum.[13] It offers an explanation of the latter as arising, even in the absence of bilayer splitting, from averaging over a distribution of local gap values under the macroscopic ARPES light spot.

Careful analysis of the STM data, combined with those of the ARPES, led us to conjecture in Ref. 9 that the observed inhomogeneous electronic structure arises from the ionic potential associated with the off-stoichiometry oxygen dopants disordered in the BiO layer. We argued that the screening of the ionic potential in the doped Mott insulator is unconventional and incomplete on the nanometer scale of the pair size, causing the local doping (hole) concentration to exhibit spatial variations. Such a doping profile results in a highly cross-correlated pairing gap profile if the pairing interaction is sufficiently short-ranged.

It should be stressed that the physics involved here is highly unconventional. In an ordinary metal, such as copper, the Thomas–Fermi screening length in the linear screening theory is shorter than 1 Å, beyond which the ionic potential is perfectly screened and the charge density homogeneous. Such a short screening length is a result of the large thermodynamic density of states or the compressibility ($dn/d\mu$) in ordinary metals. However, adding holes to a doped Mott insulator causes significant shift in the chemical potential due to the strong local Coulomb repulsion. This leads to a small electronic compressibility and thus a larger screening length even within the linear screening theory. We believe that the observed inhomogeneous superconducting state is a result of the strong local correlation in a doped Mott insulator.

It is important to provide theoretical tests for these ideas and to compare theoretical results with experiments. In this paper, we do so by studying the d-wave superconducting state of a doped Mott insulator in a microscopic theory of a generalized t-J model, where doping is accompanied by ionic Coulomb potentials centered a distance d_s away from the 2D plane. Since an exact solution of this model for large systems is not possible even numerically at present, we provide a self-consistent mean-field solution that captures the essential physics. The hope is that, upon comparing the results to experiment, we can develop useful insights to guide our understanding in the interim. Specifically, we solve a set of spatially unrestricted Bogoliubov–de Gennes equations self-consistently at every site on square lattices of up to 32×32 sites to obtain the spatial distributions of the hole concentration, the resonating valence bond, and the pairing order parameters for different nominal/average doping concentrations. We find that the inhomogeneity originates from nonlinear screening of the ionic potential. We show that a single negatively charged test ion inserted at a setback distance d_s above the 2D plane induces a nonlinear screening cloud wherein the doping concentration is significantly larger than its averaged value. For a given strength of the Coulomb interaction, the size of the nonlinear screening cloud is controlled by the distance d_s and is *independent* of the average doping concentration. With a finite density of dopant ions (the same as the averaged doped hole density), an inhomogeneous electronic structure on the scale of d_s emerges that

shares an analogy to the 2D electron system in modulation doped semiconductors, where nonlinear screening leads to an inhomogeneous mixture of metallic and dielectric regions at low electron density.[14] The immediate consequence of the nonlinear screening is the strong spatially inhomogeneous redistribution of the charge carrier density brought about by the bare ionic potential. The concept of a *local doping concentration* (LDC)[9] therefore naturally arises. The d-wave pairing amplitude turns out to follow locally the spatially varying hole density, resulting in an inhomogeneous superconducting state. In the resonating valence bond picture,[1] this corresponds to an inhomogeneous state of spinon pairing and local holon condensation. We calculate the local tunneling density of states spectrum, the integrated LDOS, and the local superconducting gap as those measured by STM. Surprisingly, the local spectral properties can be well described by the Mott–Hubbard picture once the notion of a LDC is established. We perform a detailed comparison of our results with the experimental data and find remarkable agreement in support of the conjectures made in Ref. 9 and the theoretical picture of spinon pairing with local holon condensation for the inhomogeneous superconducting state. Extending this picture to the underdoped regime, where the averaged interhole separation becomes larger than the setback distance d_s, naturally leads to percolative structures of superconducting patches immersed in a background with a large tunneling gap to single particle excitations.

Currently, there exists a "discrepancy" in the published STM data by different groups[9–11] with regard to whether the LDOS shows spatial inhomogeneity at low energies. We point out that the difference in the presented experimental data depends on whether they have been normalized to remove certain matrix element effects. In Ref. 9, we have taken into account, by correctly normalizing the data, the effect of the tunneling matrix element along the direction perpendicular to the surface. The normalized data reflect the tunneling spectra when the tip to sample distance is kept effectively at a constant. We believe this is physical. The low energy electronic spectrum as measured by the local tunneling density of states is indeed inhomogeneous.[9] In this paper, we show that the same inhomogeneity structure manifests itself at *all* energy scales in the calculated tunneling spectra. We find that the calculated zero-bias tunneling conductance, which is dominated by the nodal quasiparticles, shows spatial variations that are correlated with that of the LDC. We elucidate in detail the mapping, the differences, and similarities between the tunneling differential conductance obtained in the constant tunneling current mode, which does not directly represent the electron LDOS, and the same data normalized to reflect a constant tip-to-sample distance that faithfully represent the electronic tunneling density of states. We also provide preliminary evidence that the high superconducting transition temperature T_c can be protected by the short superconducting coherence length and coexist with this type of electronic inhomogeneity.

The rest of the paper is organized as follows. In Sec. II, we describe our generalized t-J model and set up the self-consistent equations for the spatially unrestricted Hartree-Fock-Bogoliubov mean-field solutions. In Sec. III, we study

the screening properties of the ionic potential in detail. A single test ion is inserted which imposes a Coulombic potential on the otherwise uniform *d*-wave superconducting state. The charge redistribution and the response of the pairing order parameter to screening of the ionic potential is analyzed. In Sec. IV, we discuss the solution of the inhomogeneous *d*-wave superconducting state for a finite density of dopant ions and doped holes. We emphasize the concept of LDC and analyze the distribution of the *d*-wave order parameter and its correlation with the local hole concentration in Subsection IV A. The numerical results of the local tunneling spectrum are presented in Subsection IV B and compared to experimental data. We analyze the statistical properties of the LDC, the integrated LDOS and the pairing gap distribution, and the spatial correlation and cross-correlation among these physical observables. In Sec. V, we focus on the inhomogeneity at low energy scales. We study the spatial distribution of the zero-bias tunneling conductance, its correlation with the LDC, and make predictions for experimental tests. In Sec. VI, we discuss the mapping between constant-current differential tunneling conductance and the constant tip-to-sample distance LDOS spectra. The STM topography is calculated for our system together with the constant-current differential tunneling conductance and compared to experiments. A summary of the results and their implications is given in Sec. VII together with discussions of several open issues.

II. GENERALIZED t-J MODEL AND THE SELF-CONSISTENCY EQUATIONS

We begin with the generalized t-J model Hamiltonian that includes the long-range Coulomb interaction and the ionic potentials introduced by the process of carrier doping,

$$H = H_{t\text{-}J} + H_{\text{Coul}} + H_{\text{ion}}. \tag{1}$$

Here $H_{t\text{-}J}$ is the usual 2D t-J model on a square lattice,

$$H = -t \sum_{\langle i,j \rangle} (c_{i\sigma}^\dagger c_{j\sigma} + \text{h.c.}) + J \sum_{\langle i,j \rangle} \left(\mathbf{S}_i \cdot \mathbf{S}_j - \frac{1}{4} n_i n_j \right), \tag{2}$$

where $c_{i\sigma}^\dagger$ is the electron creation operator and $\mathbf{S}_i$ is the spin operator $\mathbf{S}_i = (\frac{1}{2}) c_{i\alpha}^\dagger \vec{\sigma}_{\alpha\beta} c_{i\beta}$. The sums over $\langle i,j \rangle$ are among nearest neighbors and sums over repeated spin indices are implied. The most important Mott–Hubbard physics, i.e., the strong on-site Coulomb repulsion, is included in the additional constraint of no double occupancy at each site, $n_i = c_{i\sigma}^\dagger c_{i\sigma} \leq 1$. H_{Coul} is the long-range Coulomb repulsion,

$$H_{\text{Coul}} = \sum_i V_i n_i, \quad V_i = V_c \sum_{j \neq i} \frac{n_j - \bar{n}}{|\mathbf{r}_i - \mathbf{r}_j|}, \tag{3}$$

where $\bar{n}$ denotes the average density. The Coulomb interaction strength V_c is given by $V_c = e^2/4\pi\epsilon a$, with $\epsilon \simeq 8$ the dielectric constant[15] and $a \sim 3.8$ Å the lattice constant corresponding to the Cu–Cu atomic spacing. The resulting $V_c \sim t$. As emphasized in Ref. 16, the inclusion of the long-range Coulomb interaction is necessary to prevent the mean-field ground state of $H_{t\text{-}J}$ from macroscopic phase separa-

tion in the interesting parameter regime.[17] The off-plane ionic potential of the dopants is described by H_{ion},

$$H_{\text{ion}} = \sum_i U_i n_i, \quad U_i = \sum_{\text{ion}=1}^{N_{\text{ion}}} \frac{V_{\text{ion}}}{\sqrt{|\mathbf{r}_i - \mathbf{r}_{\text{ion}}|^2 + d_s^2}}. \tag{4}$$

Here d_s is the distance between the CuO$_2$ plane and the BiO layer where the negatively charged ions reside randomly at $\mathbf{r}_{\text{ion}}$, and N_{ion} is the number of independent ions in the BiO layer. To model the situation in BSCCO, where each dopant oxygen gives one hole to each of the planes in a bilayer, we use $N_{\text{ion}} = N_{\text{hole}} = x \times N_s$, where N_{hole} is the number of doped holes, x is the *average* doping (hole) concentration on a lattice of N_s sites. We use J as the unit of energy and set $d_s = 1.5a$, $V_{\text{ion}} = V_c = 5J$, and $t = 3J$ in most of our numerical calculations. We verified that varying these parameter in a reasonable range does not qualitatively change our results.

It is convenient to describe the projected Hilbert space in terms of a spin-carrying fermion, the spinon $f_{i\sigma}^\dagger$, creating the singly occupied site with spin-σ and a spinless boson, the holon b_i, keeping track of the empty site.[18] The electron creation operator becomes $c_{i\sigma}^\dagger = f_{i\sigma}^\dagger b_i$ and the occupancy constraint translates in this slave-boson formulation into $f_{i\sigma}^\dagger f_{i\sigma} + b_i^\dagger b_i = 1$. In the mean-field theory, the antiferromagnetic spin-exchange term is decoupled according to[19]

$$\mathbf{S}_i \cdot \mathbf{S}_j = -\tfrac{3}{8}[\chi_{ij}^* f_{i\sigma}^\dagger f_{j\sigma} + \text{h.c.} + \Delta_{ij}^*(f_{i\downarrow}f_{j\uparrow} - f_{i\uparrow}f_{j\downarrow}) + \text{h.c.}]$$
$$+ \tfrac{3}{8}(|\chi_{ij}|^2 + |\Delta_{ij}|^2),$$

where Δ_{ij} and χ_{ij} are the spinon pairing and bond order parameters respectively,

$$\Delta_{ij} = \langle f_{i\downarrow}f_{j\uparrow} - f_{i\uparrow}f_{j\downarrow} \rangle, \quad \chi_{ij} = \langle f_{i\sigma}^\dagger f_{j\sigma} \rangle, \tag{5}$$

defined for each nearest neighbor bond. The inhomogeneous superconducting phase is reached through the local condensation of bosons at low temperatures,

$$\langle b_i^\dagger \rangle = \langle b_i \rangle = \bar{b}_i. \tag{6}$$

It is important to emphasize that in the presence of the translation symmetry breaking ionic potential in Eq. (4), $(\Delta_{ij}, \chi_{ij}, \bar{b}_i)$ become spatially dependent and must be determined at every site self-consistently. Note that the local doped hole density or the LDC is then directly related to the local boson condensate density,

$$x_i = \bar{b}_i^2, \tag{7}$$

and the constraint at the mean-field level becomes $n_i^f = f_{i\sigma}^\dagger f_{i\sigma} = 1 - x_i$, which is enforced on average at every site by locally shifting the fermion chemical potential μ_f to $\lambda_i + \mu_f$. Throughout this paper, we use x to denote the average (doped) hole density or the nominal doping concentration,

$$x = \frac{1}{N_s} \sum_{i=1}^{N_s} x_i. \tag{8}$$

The decoupled Hamiltonian can be written down using the Bogoliubov–Nambu formalism over the Hilbert space of paired spinons,

$$H = \sum_{i,j} (f_{i\uparrow}^{\dagger}, f_{i\downarrow}) \begin{pmatrix} K_{ij} & F_{ij} \\ F_{ji}^{*} & -K_{ji}^{*} \end{pmatrix} \begin{pmatrix} f_{j\uparrow} \\ f_{j\downarrow}^{\dagger} \end{pmatrix}, \qquad (9)$$

where the sums on i and j run over all lattice sites and

$$F_{ij} = \frac{3}{8} J \Delta_{ij} \sum_{\eta} \delta_{j,i+\eta}, \qquad (10)$$

$$K_{ij} = -\left(t\bar{b}_i^2 + \frac{3}{8} J \chi_{ij} \right) \sum_{\eta} \delta_{j,i+\eta} + [V_{\mathrm{sc}}(i) - \mu_f] \delta_{ij}, \qquad (11)$$

with $\eta = \pm\hat{x}, \pm\hat{y}$. In Eq. (11), $V_{\mathrm{sc}}(i)$ given by

$$V_{\mathrm{sc}}(i) = U_i + \lambda_i + V_c \sum_{j \neq i} \frac{\bar{b}_j^2 - x}{|\mathbf{r}_i - \mathbf{r}_j|}, \qquad (12)$$

is the nonlinearly screened local potential seen by the spinons implied by the self-consistency conditions. Note that in deriving Eq. (12), only the Hartree potential in the long-range Coulomb interaction is retained, whereas the exchange potential is neglected. The effects of the latter on the super-conducting state will be studied elsewhere.

The Hamiltonian in Eq. (9) can be diagonalized in real space by solving the corresponding Bogoliubov–de Gennes equations to obtain the eigenstates $\gamma_n^{\dagger}$ and γ_n with energy $E_n, n = 1, \ldots, 2N_s$. The spinon operator can be expanded in this basis according to

$$f_{i\uparrow}^{\dagger}(t) = \sum_n u_n(i) \gamma_n^{\dagger} e^{-iE_n t/\hbar}, \qquad (13)$$

$$f_{i\downarrow}(t) = \sum_n v_n(i) \gamma_n^{\dagger} e^{-iE_n t/\hbar}, \qquad (14)$$

where $[u_n(i), v_n(i)]$ is the wave function at site i. The order parameters and the local hole density can be expressed in terms of the wave functions as follows:

$$\Delta_{ij} = \sum_n [v_n^*(i) u_n(j)[1 - f(E_n)] - u_n(i) v_n^*(j) f(E_n)], \qquad (15)$$

$$\chi_{ij} = \sum_n [v_n^*(i) v_n(j)[1 - f(E_n)] + u_n(i) u_n^*(j) f(E_n)], \qquad (16)$$

$$1 - x_i = \sum_n [|v_n(i)|^2 [1 - f(E_n)] + |u_n(i)|^2 f(E_n)], \qquad (17)$$

where $f(E_n)$ is the usual Fermi distribution function.

We solve the self-consistency Eqs. (9)–(17) through numerical iterations. Typically, we start with a random set of $(\Delta_{ij}, \chi_{ij}, \lambda_i, x_i, \mu_f)$, insert them into Eq. (9), and diagonalize

the resulting matrix to obtain the wave functions $[u_n(i), v_n(i)]$ and the eigenvalues E_n. Then we update the set of $(\Delta_{ij}, \chi_{ij}, \lambda_i, x_i, \mu_f)$ according to Eqs. (15), (16), (17) and insert them back into the Hamiltonian (9). The procedure is iterated until convergence is reached. In general, we allow χ_{ij} and Δ_{ij} to be complex at the beginning of the iteration, but both of these order parameters converge to real values at the end of the iteration in the average doping range ($0.06 < x < 0.32$) studied.

In order to compare to STM data, we calculate the local *tunneling* density of states,

$$N_i(\omega) = \mathrm{Im} \int dt e^{i\omega t} G_{ii}^{\mathrm{ret}}(t), \qquad (18)$$

where $G_{ii}^{\mathrm{ret}}(t)$ is the *retarded* local Green's function of the *electrons*,

$$G_{ii}^{\mathrm{ret}}(t) = -\theta(t) \langle \{ c_{i\sigma}^{\dagger}(0), c_{i\sigma}(t) \} \rangle. \qquad (19)$$

In the mean-field theory, since the bosons locally condense, we have

$$G_{ii}^{\mathrm{ret}}(t) = -\bar{b}_i^2 \theta(t) \langle \{ f_{i\sigma}^{\dagger}(0), f_{i\sigma}(t) \} \rangle. \qquad (20)$$

Notice that the local electron Green's function and therefore the local tunneling density of states is equal to the local holon condensate density times the local spinon Green's function.[20] From Eq. (7), it is clear then that the LDOS is overall proportional to the LDC x_i. Using Eqs. (13), (14), we obtain

$$N_i(\omega) = x_i \sum_n [|u_n(i)|^2 \delta(\omega - E_n) + |v_n(i)|^2 \delta(\omega + E_n)]. \qquad (21)$$

The role played by the LDC is two-fold: it enters as an over-all prefactor through essentially the wave function renormalization of the electrons as well as through the LDOS of spinons from the response of Δ_{ij} and χ_{ij} to a spatially varying x_i. This is a property of the tunneling density of states which is different from the thermodynamic density of states.[21]

Our choice of the t-J model for quantitative calculations is a natural one, because it is the simplest model that captures the physics of a doped (antiferromagnetic) Mott-insulator. In this strong coupling approach, the carrier concentration is proportional to the doping concentration (rather than the electron density), which is the most fundamental property of a doped Mott-insulator. More specifically, as can be clearly seen from Eq. (20), the coherent weight of the quasiparticle is small at small doping and scales with the LDC. This is in excellent agreement with the recent ARPES measurements[13,22] on BSCCO, where the weight of the emergent quasiparticle peak below T_c near the anti-node was found to be proportional to the doping concentration at low temperatures.
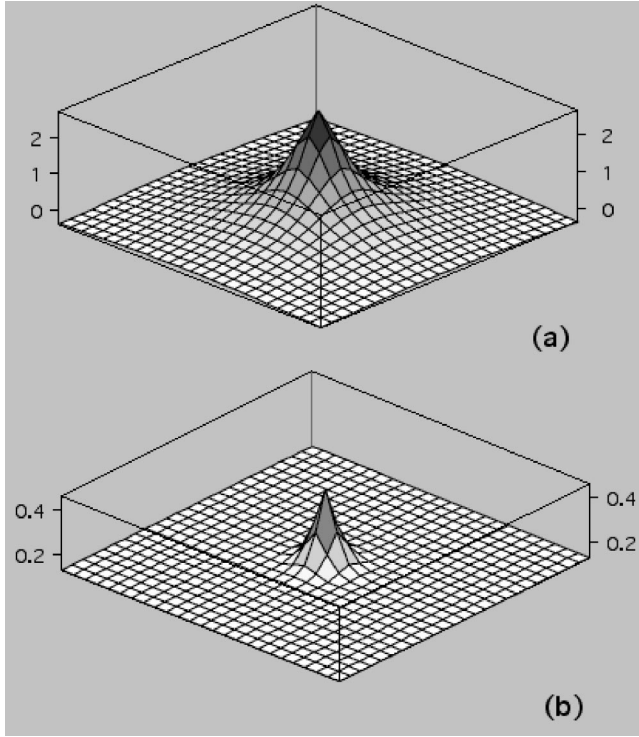
FIG. 1. The Coulomb potential from a single negatively charged ion located at a distance $d_s = 1.5a$ above the center of an otherwise uniform 2D *d*-wave superconductor. The lattice size is 25×25 and the average doping $x = 0.12$. (a) The long-range bare ionic potential from Eq. (4). (b) The screened potential from Eq. (12).

III. A SINGLE OFF-PLANE ION AND NONLINEAR SCREENING

To understand the screening properties of the ionic potential better, we start with the case where a single off-plane ion (i.e., $N_{ion} = 1$) is placed above the center of a 25×25 lattice with a setback distance $d_s = 1.5a$. The ion imposes a Coulomb potential on the otherwise uniform superconducting state at a doping level x. This situation is similar to that of a single nonmagnetic impurity (say Zn) extensively studied using the t-J model recently,[23–25] except that the impurity is located out of the plane and the impurity potential is long-ranged. The scattering is presumably *not* in the unitary limit. In addition, fully self-consistent solution in ($\bar{b}_i$, Δ_{ij}, χ_{ij}) has not been studied before.

Figure 1 shows the bare ionic potential U_i from Eq. (4) and the screened potential $V_{sc}(i)$ from Eq. (12) coming out of the self-consistent solution. The average doping concentration in the plane is $x = 0.12$. It is clear that the long-range impurity potential in Fig. 1(a) is perfectly screened at distances much larger than d_s but poorly screened at short distances resulting in a short-range impurity potential in Fig. 1(b).

The nature of the screening is revealed when we look at the redistribution of the carrier density as a result of screening. The self-consistently determined local hole concentration x_i is plotted in a 2D hole density map in Fig. 2(a), which shows that in the vicinity of the dopant ion, the hole density is strongly inhomogeneous, namely the changes in the hole concentration δx_i, brought about by the dopant ionic poten-
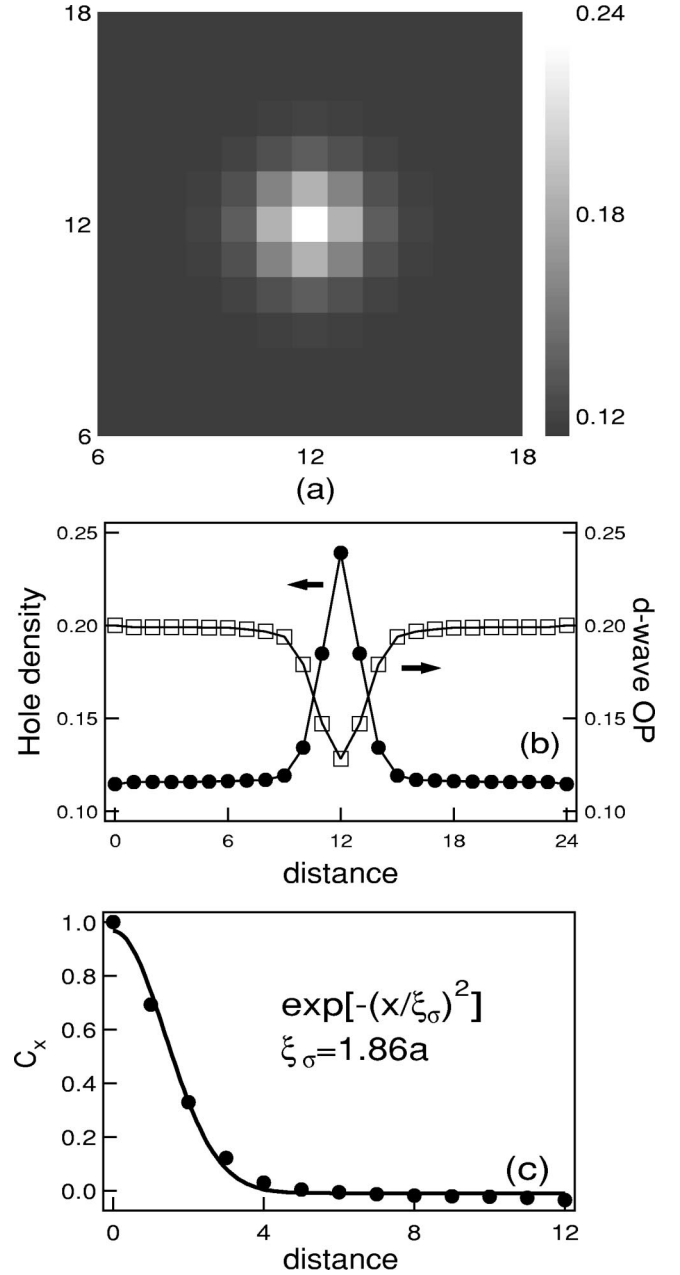

FIG. 2. Spatial variations of the LDC induced by the ionic potential in Fig. 1. (a) The 2D plot of the local hole density (x_i) redistribution as a result of nonlinear screening. (b) The hole density and the corresponding *d*-wave pairing order parameter (OP) along a horizontal line-cut passing through the center of the 25 $\times 25$ lattice at $x = 0.12$. (c) The azimuthally averaged autocorrelation function of the spatial variations in local hole concentration δx_i defined in Eq. (22). The solid line is a Gaussian fit to the data, which gives a decay length $\xi_\sigma = 1.86a$.

tial, are comparable to the averaged concentration x itself. Figure 2(b) shows the hole density distribution along a horizontal line-cut passing through the center of the lattice. This clearly demonstrates that the screening of the ionic impurity potential in the doped Mott-insulator is highly unconventional and is entirely dominated by nonlinear screening[14] on the scale of the ionic setback distance d_s. The nonlinearity

in screening is further verified by its nonlinear response to changes in the strength of the Coulomb potential V_{ion}. It is instructive to compare to conventional screening in the linear response theory described by the Thomas–Fermi screening length, which is applicable to ordinary metals and superconductors. For an electron gas in 2D, the Thomas–Fermi screening length is *independent of electron density* and is given by $q_{\text{TF}}^{-1} = a_B^*/2$, where $a_B^* = \hbar^2\epsilon/m^*e^2$ is the effective Bohr radius.[26] Taking $\epsilon \simeq 8$ and a thermodynamic effective mass $m^*/m \sim 3$, which is appropriate for the cuprates, gives $a_B^* \simeq 1.4$ Å . The resulting Thomas–Fermi screening length ~ 0.7 Å which is much less than a lattice spacing $a \simeq 3.8$ Å . Thus linear screening theory would have predicted that the ionic Coulomb potential is screened on the length scale of a lattice spacing and the charge redistribution induced by the bare potential is small. In our case, Figs. 2(a) and 2(b) clearly show that linear screening is only valid when the distance to the center of the ionic potential is much greater than the distance d_s, where the hole density is essentially uniform and its value close to the average concentration $x = 0.12$.

Thus, the profile of the screened impurity potential and that of the hole density distribution and, as we shall see later, that of the d-wave pairing OP [see Fig. 2(b)], are controlled by the crossover from nonlinear to linear screening as one moves away from the center of the ionic potential. To better quantify this crossover behavior, we study the autocorrelation function of the local hole density variations $\delta x_i = x_i - x$,

$$C_x(\mathbf{r}_j) = \frac{1}{N_s}\sum_i \langle \delta x_i \delta x_{i+j}\rangle. \tag{22}$$

In Fig. 2(c), we show the azimuthally averaged C_x, which decays very fast with the distance, indicative of strong short-range correlation in the LDC. The short-distance behavior can be fitted very well by a Gaussian with a decay length $\xi_\sigma = 1.86a$. For convenience, let us define the correlation length by the decay length of the Gaussian function. We arrive at a hole-density correlation length $\xi_x = 1.86a$, which is quite close to the setback distance $d_s = 1.5a$, suggesting the latter as the length scale over which the crossover between linear and nonlinear screening takes place.

We next study the average doping dependence of the screening in the nonlinear regime. In the linear screening theory, the fact that the 2D Thomas–Fermi screening length is independent of carrier density is a consequence of the properties of the density of states and the polarizability of the 2D electron system.[26] This suggests that the insensitivity of screening to carrier concentration in 2D should be true even for nonlinear screening. Analytical solutions of the 2D nonlinear screening problem only exists for the special case of an antidot in a semiconductor 2D electron gas in the continuum.[27] To study this question in the d-wave superconducting state of a doped Mott-insulator in the presence of a periodic lattice potential, we plot, in Fig. 3(a), the variation of the local hole density from its average value (δx_i) as a function of distance along the center horizontal cut for several different average hole concentrations. The fact that the data points almost completely collapse onto a single curve
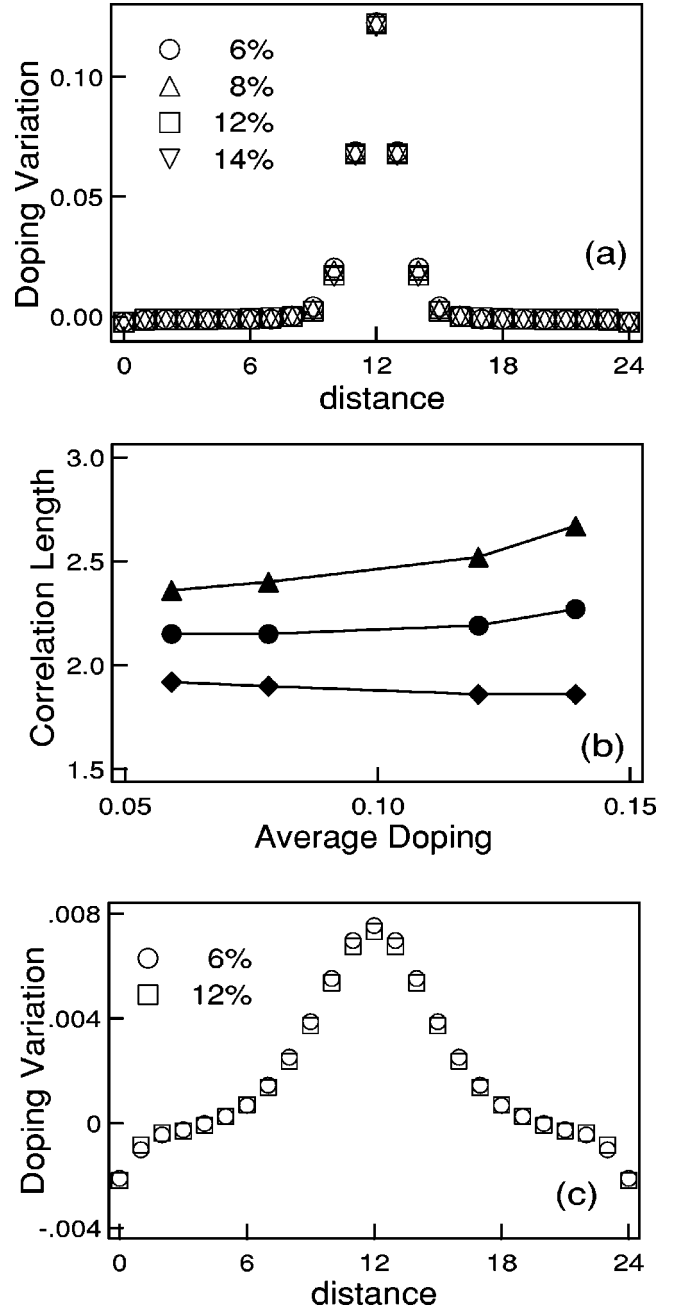

FIG. 3. The average doping and setback distance dependence of screening. (a) The spatial variations in hole concentration (δx_i) along the central line-cut at four different average doping concentrations, showing screening is insensitive to average doping x. (b) The decay lengths of the hole-density (diamonds) and the d-wave pairing OP (triangle) autocorrelations, and that of the cross-correlation (circle) between the two as a function of average doping x. (c) Same as in (a), but for a larger setback distance $d_s = 5a$.

shows that the screening is indeed insensitive to the carrier density in both the linear and the nonlinear screening regime. This is verified quantitatively by the very weak doping dependence of the decay lengths extracted from the Gaussian fits to the correlation functions at the corresponding doping levels, shown in Fig. 3(c). Thus, for a given strength of the ionic Coulomb potential, the size of the nonlinear screening
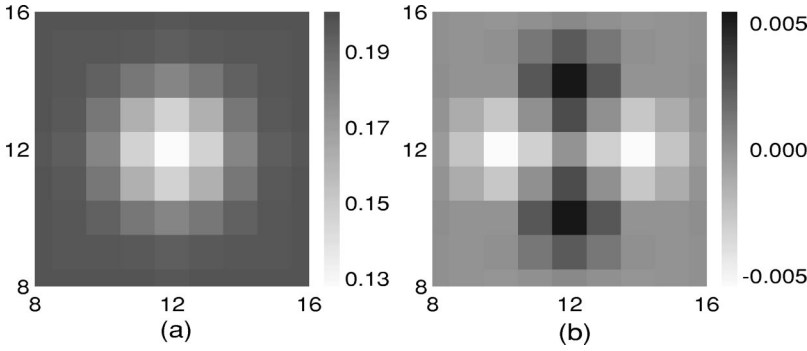
FIG. 4. The 2D maps showing the spatial variations in the dominant *d*-wave (a), and the accompanying extended s-wave (b) pairing OPs in the vicinity of the ionic potential.

cloud around the center of the potential is controlled entirely by the setback distance d_s. In Fig. 3(c), we show the spatial variation of the LDC δx_i along the center horizontal cut for the case of a larger setback distance $d_s = 5a$ at $x = 0.06$ and 0.12. It is clear that as the screened potential becomes smoother, the size of the screening cloud becomes larger, characterized by a decay length on the order of d_s.

In Fig. 4, we show the spatial variation of the self-consistently determined superconducting order parameter near the center of the ionic potential for $d_s = 1.5a$. We find that the nonlinear screening region where the hole concentration exhibits strong inhomogeneity is accompanied by spatial variation of the order parameter Δ_{ij}. Moreover, when Δ_{ij}, defined in Eq. (5), is decomposed into a $d_{x^2-y^2}$ and an extended s-wave component at a site i according to

$$\Delta_d(i) = \tfrac{1}{4}(\Delta_{i,i+\hat{x}} + \Delta_{i,i-\hat{x}} - \Delta_{i,i+\hat{y}} - \Delta_{i,i-\hat{y}}), \quad (23)$$

$$\Delta_s(i) = \tfrac{1}{4}(\Delta_{i,i+\hat{x}} + \Delta_{i,i-\hat{x}} + \Delta_{i,i+\hat{y}} + \Delta_{i,i-\hat{y}}), \quad (24)$$

we find that the spatially varying *d*-wave order parameter $\Delta_d(i)$ shown in Fig. 4(a) is complimented by a much smaller nonuniform $\Delta_s(i)$ shown in Fig. 4(b). The magnitude of Δ_d along the center line-cut in Fig. 4(a) has been shown in Fig. 2(b).

This situation is quite reminiscent of a single *in-plane* nonmagnetic impurity, e.g., an intentionally doped Zn atom, that replaces a copper atom causing strong scattering in the unitary limit.[23–25,28,29] The inhomogeneity induced Δ_s shows an interesting four-fold (*d*-wave) symmetry, i.e., it is vanishingly small along the nodal direction of $\Delta_d(i)$ and changes sign upon a 90° rotation. These properties can be qualitatively understood from the Ginzburg–Landau theory[23,30] that permits by symmetry a mixed gradient term proportional to

$\partial\Delta_d\partial\Delta_s$. Note that the order parameters in this $d+s$ state are both real and that spontaneous time-reversal symmetry breaking, such as in a $d+is$ state, does not occur. It is interesting to point out that the reduction is greater in the anti-nodal direction where the *d*-wave gap is at its maximum.

The autocorrelation function of the spatial variation of the *d*-wave OP $\delta\Delta_d(i) = \Delta_d(i) - \bar{\Delta}_d$ and the cross-correlation function between $\delta\Delta_d(i)$ and the local doping variation δx_i are defined by

$$C_{\Delta_d}(\mathbf{r}_j) = \frac{1}{N_s}\sum_i \langle \delta\Delta_d(i)\,\delta\Delta_d(i+j)\rangle, \quad (25)$$

$$C_{x-\Delta_d}(\mathbf{r}_j) = \frac{1}{N_s}\sum_i \langle \delta x_i\,\delta\Delta_d(i+j)\rangle. \quad (26)$$

We plot the azimuthally averaged correlation functions in Figs. 5(a) and 5(b). The Δ_d-correlation length $\xi_{\Delta_d} \simeq 2.53a$, which is close to the hole density correlation length. The fact that the cross-correlation length, $\xi_{x-\Delta_d} \simeq 2.26a$, is close to ξ_x and ξ_{Δ_d} shows that the spatial variations in Δ_d and the LDC are strongly (anti-)correlated. This is an important character of the *d*-wave superconducting state emerged from the short-range resonating valence bond state,[1,31] where the local spinon pairing produced by the nearest-neighbor antiferromagnetic exchange interaction is directly affected by the local holon condensate density.

To summarize this section, an out-of-plane negatively charged ion induces a nonlinear screening cloud in its vicinity, wherein the doping concentration is significantly higher and the *d*-wave pairing parameter significantly smaller than their averaged values in the bulk of the 2D superconductor.
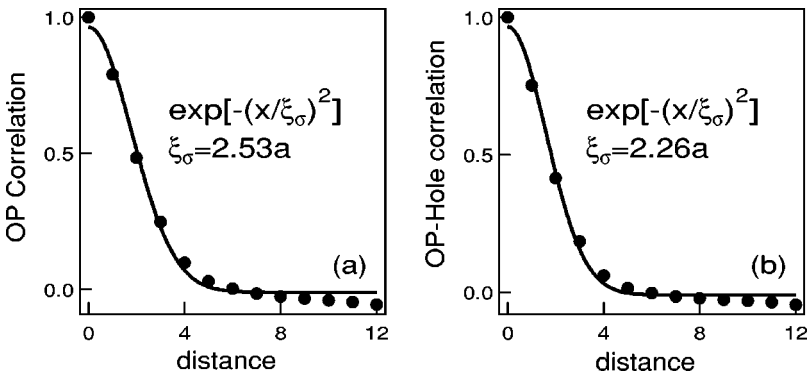

FIG. 5. The azimuthally averaged autocorrelation function for the *d*-wave OP variation (a) and the *absolute* value of the cross-correlation function between the hole density variation and the *d*-wave OP variation (b). The solid lines are Gaussian fits to the data.

The size of the nonlinear screening cloud is essentially independent of the averaged doping concentration. It is controlled by the setback distance d_s of the dopant ions to the 2D plane. This local picture for the response of the d-wave superconducting state to a single ionic test charge will be important for understanding the real situations of many ions, particularly in the case of dilute dopants in the underdoped regime. In the rest of the paper, we use $d_s = 1.5a$. This comes out naturally from the lattice constants of BSCCO which is about 3.8 Å in the plane and 5 Å in the c-direction. We will come back to this issue in the last section and discuss other physical processes, such as dielectric screening from interband transitions and electron-phonon coupling, that could complicate the choice of d_s, but would not change the essential physics described in this paper.

IV. FINITE DENSITY OF IONS—INHOMOGENEOUS SUPERCONDUCTING STATE OF A DOPED MOTT-INSULATOR

Having studied how an external out-of-plane charge is screened by the d-wave superconductor, we now turn to the situation in BSCCO where N_{ion} number of negatively charged ions resides in the BiO layer donating $N_{\text{hole}} = N_{\text{ion}}$ number of doped holes to each of the CuO bilayers. Without the knowledge of the detailed chemical frustration encountered by the dopant ions, we assume that they distribute randomly in the BiO layer. This can lead to accidental clustering of the dopant oxygen atoms which may or may not happen in real materials depending on the details of the chemistry. Since very strong clustering happens rarely and locally, it does not affect the essential physics we describe.

A. Inhomogeneous electronic structures

The bare ionic potential calculated from Eq. (4) is shown in Fig. 6(a) for a 32×32 lattice at $x = 0.12$. The self-consistently determined screened potential of Eq. (12) is plotted in Fig. 6(b). The large fluctuations in the bare ionic potential are dramatically screened as can be seen by comparing Fig. 6(a) and 6(b). The spatial variations of the self-consistently determined LDC in Eq. (7) and Δ_d in Eq. (23) are shown as 2D maps in Figs. 7(a) and 7(b). It is clearly seen from Fig. 7(a) that the variations in the hole density closely track the screened potential in Fig. 6(b). The local ionic dopant configurations are shown as black dots. The reverse color-coding for the Δ_d-map makes it easy to observe the (anti-)correlation between x_i and $\Delta_d(i)$. The average inter-hole distance at this doping is $d_x \simeq 2.86a$, which is smaller than the size of the screening cloud $2\xi_x \simeq 3.72a$ of a single isolated ion discussed in the previous section. The fact that the number of dopant ions is the same as the number of doped holes then implies that the screening clouds associated with individual ions overlap and interfere such that nonlinear screening dominates and leads to significant inhomogeneity in the electronic structure throughout the entire system. This confirms the conjecture we made in Ref. 9 that the inhomogeneity results from the lack of conventional metallic screening of the dopant ionic potential in doped Mott-insulators.
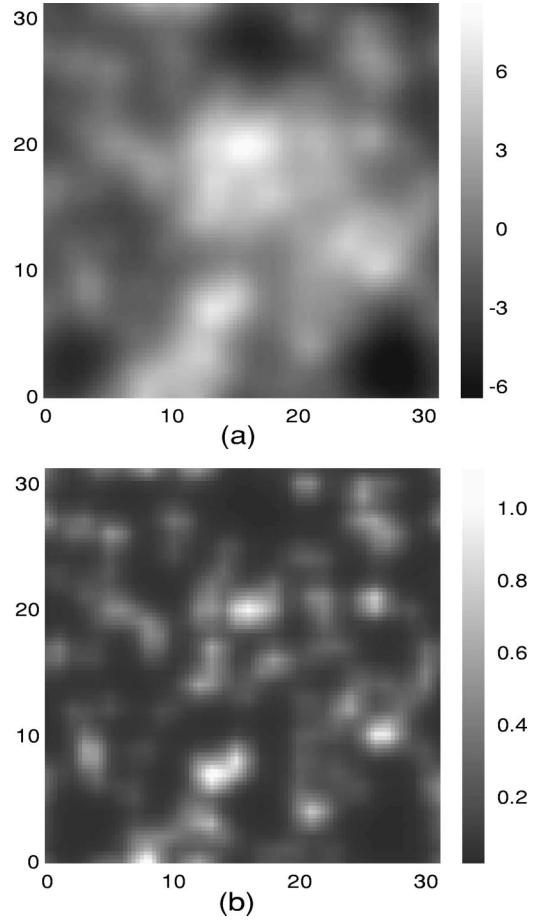

FIG. 6. 2D density plot of the bare (a) and the screened (b) ionic potential on a 32×32 lattice at average doping $x = 0.12$. The data have been smoothed to reduce the effects of the lattice discreteness.

We present, in Fig. 8, the autocorrelation and cross-correlation function analyses for the variations in LDC and the d-wave OP defined in Eqs. (22),(25),(26). The 2D hole–hole correlation is plotted in Fig. 8(a), which shows a rapidly decaying central peak and a weak interference pattern at larger distances due the presence of many-ionic impurities and the d-wave gap structure. Taking the azimuthal average of Fig. 8(a) results in Fig. 8(b). The decay length extracted from a Gaussian fit is $\xi_x = 1.8a$, very close to that of the isolated ion case discussed in the previous section. This indicates that the main effects controlling the average size of the ''patches'' come from the single ion screening cloud. The weak oscillatory structures at larger separations is a result of the interference pattern in Fig. 8(a). The distance to the first weak secondary peak can be interpreted as the averaged distance between regions or patches where the x_i and $\Delta_d(i)$ vary significantly from their averaged values.

The azimuthally averaged autocorrelation for the d-wave order parameter variations is plotted in Fig. 8(c), which shows the same structure with a decay length $\xi_{\Delta_d} \simeq 2.2a$. We remark that at this average hole concentration, which is slightly below optimal doping, the oscillatory structures are rather weak and are just beginning to emerge. Interestingly, the azimuthally averaged correlation functions obtained from
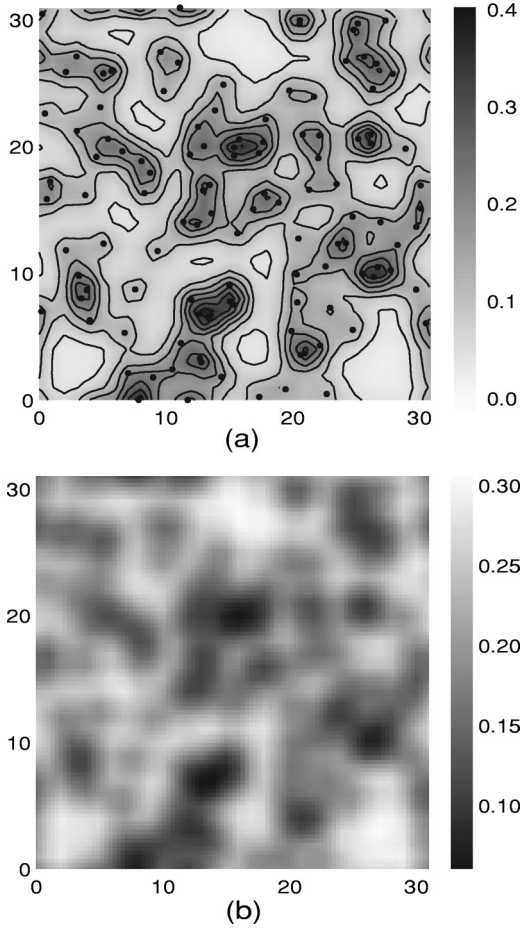
(a)

(b)

FIG. 7. The spatial variations of the local hole concentration x_i (a) and the d-wave order parameter $\Delta_d(i)$ (b) shown as 2D maps for $x=0.12$ on a 32×32 lattice. The location of the negatively charged ions projected on the 2D plane is shown as black dots in (a), together with the contours of the doped hole density. Reversed color-coding is used in (b) for easy visualization of the anti-correlation between x_i and $\Delta_d(i)$.

the experimental STM data on optimally doped BSCCO, shown in Figs. 2(e)–2(f) of Ref. 9, have the same structure, including the weak oscillations in the tails. We expect the secondary peak to develop more prominently in more underdoped systems where percolativelike patches are likely to become more pronounced with increasing average inter-hole distance.

Comparison of the x_i-map in Fig. 7(a) and the Δ_d-map in Fig. 7(b) shows that the order parameter gap is bigger where the doping rate is lower and vice versa, in agreement with the general trend of the doping dependence of Δ_d in a clean system. This (anti-)correlated behavior is confirmed by the cross-correlation analysis of δx_i and $\delta\Delta_d$ in Fig. 8(d), where the *absolute* value of the azimuthally averaged correlation function is plotted versus separation. The fact that the cross-correlation length, $\xi_{x-\Delta_d}\simeq2.1a$, is very close to that of the auto-correlations indicates that the correlation between the spatial variations in Δ_d and x_i is very strong.

We proposed, in Ref. 9, the concept of *local doping concentration* to emphasize the local nature of the physics asso-

ciated with screening and pairing in a doped Mott-insulator. To further substantiate this idea, we produce a scatter plot of the local d-wave order parameter $\Delta_d(i)$ versus the local doping x_i in Fig. 9(a). For a range of doping near the average doping value of $x=0.12$, the data points scatter around the Δ_d vs x curve (solid line) obtained in the homogeneous case without the ionic dopant potential. In the regions where the local doping is low, the scatter in Δ_d is small and the correlation between $\Delta_d(i)$ and x_i is extremely strong. On the other hand, the $\Delta_d(i)$ values show significant scatter in the locally overdoped regimes and deviate appreciably from the values in a clean system at the corresponding doping level. Also shown in Fig. 9(a) is the scatter plot of the much smaller, extended s-wave order parameter $\Delta_s(i)$ versus x_i. It scatters around a zero mean and shows a slightly larger variance with decreasing LDC. The statistical distribution of Δ_d in this single 32×32 system is plotted as histograms in Fig. 9(b). It can be fitted reasonably well by a Gaussian distribution.

B. Local tunneling density of states as measured by STM spectroscopy

To enable further comparisons with the STM experiments, we next calculate the local tunneling density of states $N_i(\omega)$ according to Eq. (21). The δ functions in Eq. (21) are replaced by the derivatives of the corresponding Fermi distribution function[32] at an inverse temperature of $\beta J=30$. Parallel to our presentation of the experimental data,[9] we extract the local pairing energy gap (full gap), denoted by $\Delta_T(i)$ to differentiate from the d-wave OP $\Delta_d(i)$ discussed above, from the peak-to-peak distance in the electron LDOS spectrum $N_i(\omega)$ at every site i. Simultaneously, we obtain the integrated LDOS (ILDOS) at every site i from

$$I_i=\int_{-\omega_0}^{0}d\omega N_i(\omega), \tag{27}$$

where the integration limit is typically taken to be $-\omega_0=-J$. Note that $N_i(\omega)$ at $\omega<0$ corresponds to the LDOS of the occupied states below the chemical potential. It should be compared to the STM tunneling spectrum at *negative sample bias* where electrons tunnel out of the occupied states in the sample. The energy ω is related to the bias V according to $\omega=eV$.

The spatial variations of $\Delta_T(i)$ and I_i are shown as the gap and the ILDOS maps in Figs. 10(a) and 10(b), respectively. As used in Ref. 9, the reverse color coding in the gap map (brighter color for a smaller tunneling gap) makes it easy to observe its (anti-)correlation with the ILDOS map, namely, bigger gap regions correspond to smaller ILDOS and vice versa, in agreement with the STM data. In Fig. 11(a), we construct a scatter plot of the superconducting gap versus the ILDOS consisting of a total of $32\times32=1024$ data points, which suggests an approximate linear relationship between the two quantities, in remarkable agreement with the STM data we presented in Fig. 4 of Ref. 9.

It is easy to notice the great similarity between the ILDOS map in Fig. 10(b) and the 2D hole density map shown in Fig. 7(a). This supports within our model the conjecture made in
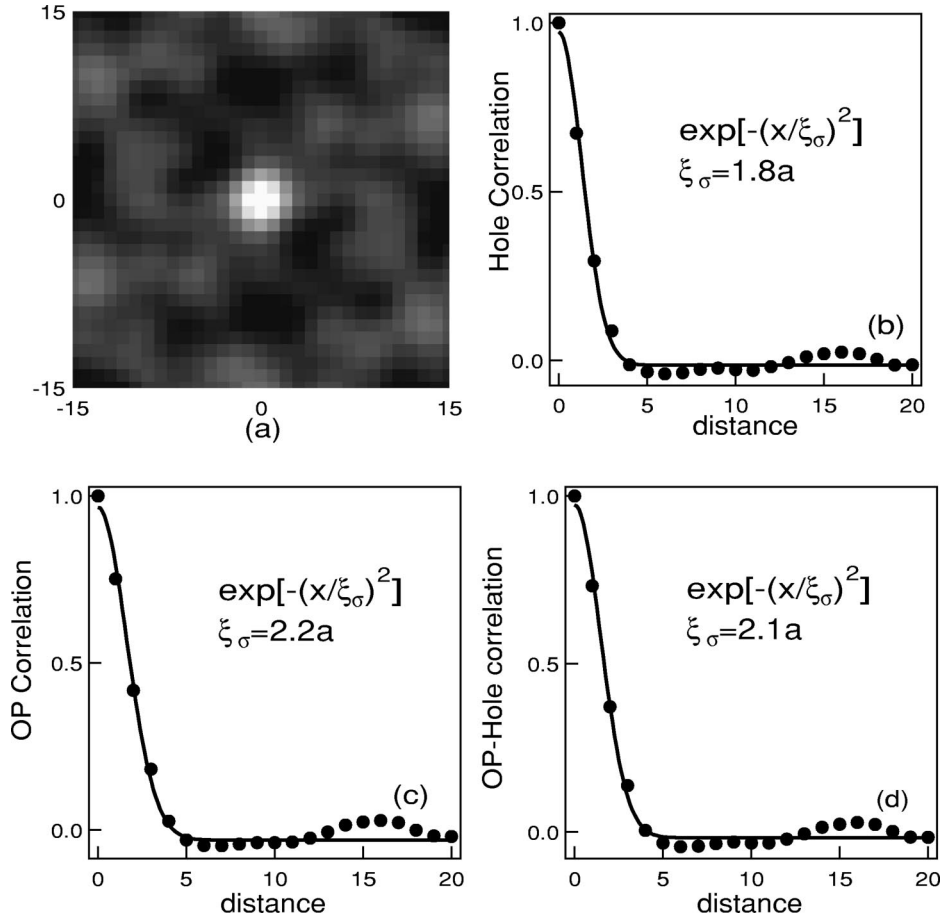
FIG. 8. The autocorrelation and cross-correlation analysis of the spatial variations in the doping concentration δx_i and the d-wave order parameter $\delta\Delta_d(i)$. (a) 2D autocorrelation of δx_i. (b) Azimuthally averaged autocorrelation function of δx_i. (c) Azimuthally averaged autocorrelation function of $\delta\Delta_d(i)$. (d) The absolute value of the azimuthally averaged cross-correlation function of δx_i and $\delta\Delta_d(i)$. The solid lines in (b), (c), and (d) are Gaussian fits to the correlation functions with the corresponding decay lengths ξ_σ shown in legends.

Ref. 9 that the ILDOS as measured by STM should be approximately proportional to the LDC.

To examine this relationship in more detail, we show a scatter plot of the ILDOS I_i, obtained from Eq. (27), versus the local doping level x_i in Fig. 11(b). Remarkably, the ILDOS is indeed linearly proportional to the LDC when x_i is small, i.e., when the local region is underdoped. This is consistent with the Mott–Hubbard picture in which doping a Mott-insulator introduces spectral weight near the Fermi energy necessary to transform the insulator into a superconductor. As observed in recent ARPES experiments,[22,13,33] the integrated quasiparticle weight scales with the average doping concentration in the underdoped regime. The idea of LDC that we advocate extends this Mott–Hubbard picture, commonly used to interpret macroscopic spectroscopy properties, to microscopic scales. It remains valid in describing the local spectroscopies of the short-coherence length superconducting state of the doped Mott-insulator. However, for larger hole concentration, i.e., further away from the Mott-insulator, the ILDOS in Fig. 11(b) tends to taper off and saturate. It shows that the two quantities are more intricately connected than the overall proportionality stemming from the quasiparticle wave function renormalization which is apparent in Eq. (21). This result turns out to be important for the analysis of the low energy inhomogeneity structures in the following section.

The statistical properties of the tunneling gap Δ_T and the ILDOS I_i are in general quite similar to those of the d-wave

pairing order parameter Δ_d and the local hole concentration x_i. The histogram of Δ_T in the 32×32 system is plotted in Fig. 12(a), which shows an approximate Gaussian distribution. The azimuthally averaged autocorrelation of the spatial gap variation $\delta\Delta_T(i)$ is shown in Fig. 12(b), and that of the cross-correlation of the gap variation and the ILDOS variation,

$$C_{I-\Delta_T}(\mathbf{r}_j) = \frac{1}{N_s}\sum_i \langle \delta\Delta_T(i)\,\delta I_{i+j}\rangle, \qquad (28)$$

is shown in Fig. 12(c) in the absolute value. The extracted gap correlation length $\xi_{\Delta_T}\simeq2.9a$ is somewhat larger than that of d-wave order parameter ξ_{Δ_d}. Although the values of the decay lengths depend on the value of the setback distance d_s of the dopant oxygen ions, we find for $d_s=1.5a$, and $a=3.8$ Å, $\xi_{\Delta_T}\simeq11$ Å which is close to the corresponding value of 14 Å obtained by analyzing the experimental data.[9] The similar cross-correlation length is consistent with the observation that these two quantities are strongly (anti-)correlated.

Next we turn to the details of the spatial variations of the local tunneling spectrum and make comparisons to experiments. Figure 13(a) shows a three-dimensional rendering of the tunneling spectra along a horizontal line-cut marked in Fig. 10, exemplifying the detailed variations of the LDOS, the pairing energy gap, and the correlation between them.
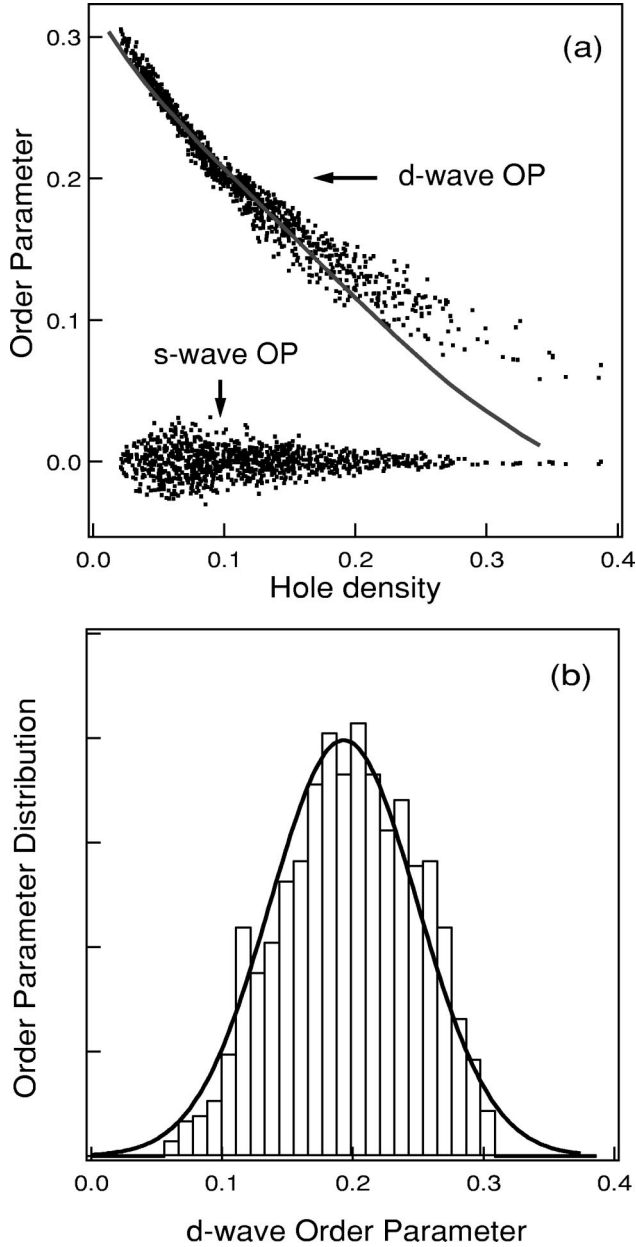
FIG. 9. (a) A scatter-plot of the *d*-wave order parameter $\Delta_d(i)$ and the extended s-wave order parameter $\Delta_s(i)$ versus local doping concentration x_i. The solid line corresponds to Δ_d as a function of x obtained in the absence of the ionic dopant potential. (b) A histogram showing the statistical distribution of $\Delta_d(i)$ in this *single* 32 ×32 system. The solid line is a Gaussian fit.

The projection of Fig. 13(a) onto the 2D plane is shown in Fig. 13(b). It is clear that regions with higher ILDOS also exhibit smaller pairing gaps and higher coherence peaks. The black dotted lines trace the positions of the coherence peaks. Combined with the gap map in Fig. 10(a), one can see that the gap varies somewhat less rapidly near the center of a "patch" than at its "edges." We expect this feature to become more prevalent for smaller average doping concentrations, i.e., more underdoped samples. In Fig. 13(c), we show five characteristic tunneling spectra calculated at the five positions marked in Fig. 10(a). The LDC at these points are
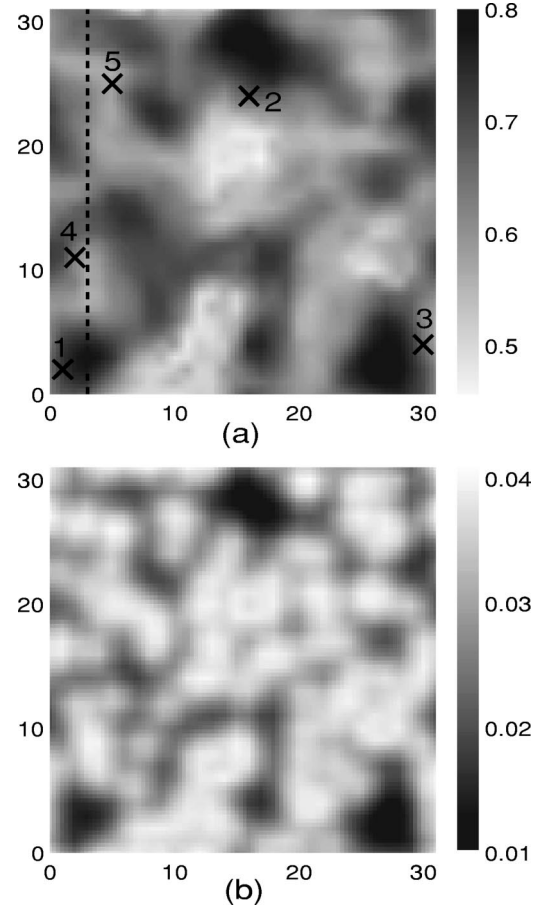

FIG. 10. The 2D tunneling gap map (a) and the ILDOS map (b). The reverse color coding in the gap map (brighter color for a smaller gap) makes it easy to observe its (anti-)correlation with the ILDOS map. The tunneling spectra along a line-cut marked by the dashed line and at the five locations marked by × in (a) are shown in Fig. 13.

given in the captions. Notice that the spectral lines plotted versus the bias voltage show remarkable resemblance to the experimental data shown in Fig. 3 of Ref. 9. The most striking feature is that the spatial inhomogeneity exists all the way down to low energies as can be clearly seen from the systematic scatter in the zero-bias tunneling conductance.[34] The broad range of agreements between the results presented in Figs. 11, 12, and 13, and the experimental findings including such details add to our confidence that the present theory of the inhomogeneous *d*-wave superconducting state with spinon pairing and local holon condensation captures the essential physics of the superconducting state in BSCCO.

V. ZERO-BIAS TUNNELING DENSITY OF STATES

One of the most striking results of both the STM measurements (see Fig. 3 of Ref. 9) and the present theory (see Fig. 13) is that the spatially inhomogeneous electronic structure not only appears at the energy scale of the superconducting gap, but persists all the way down to low energies, including the zero-bias tunneling conductance. On the experimental side, the low energy inhomogeneity can only be observed
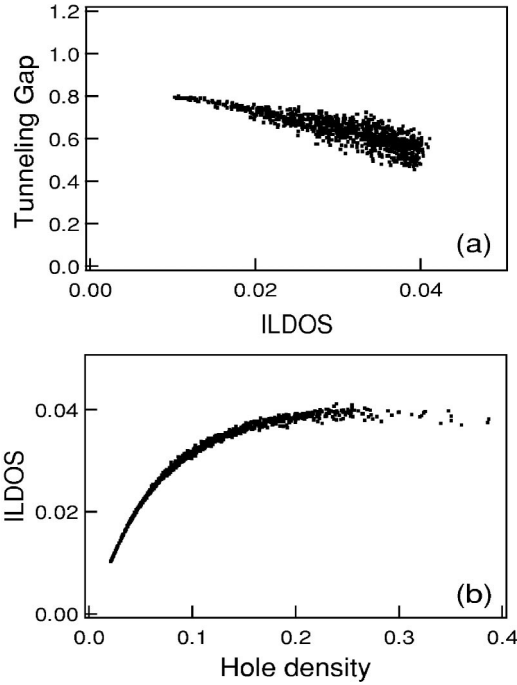
FIG. 11. (a) A scatter plot of the superconducting gap $\Delta_T(i)$ in the tunneling spectrum versus the ILDOS. (b) A scatter plot of the ILDOS versus the LDC x_i.

clearly when the tunneling matrix element effect along the c-axis is removed by a normalization procedure introduced in Ref. 9. Let's take a brief detour and study this matrix element effect. The tunneling current at site $\mathbf{r}_i$ is given by

$$I_E(\mathbf{r}_i V) = \int d\omega f(\omega)[1 - f(\omega + eV)]$$
$$\times N_i(\omega)\rho(\omega + eV)|M(\mathbf{r}_i, z)|^2, \qquad (29)$$

where $\rho(\omega)$ is the density of states of the STM tip which is usually taken to be a constant, and $M(\mathbf{r}_i, z)$ is the tunneling matrix element. Our knowledge of M is scarce in complicated materials, but in general one should be able to factor out its dependence on z which corresponds to the tip distance to the tunneling surface,

$$M(\mathbf{r}_i, z) = \text{const.} \times m(\mathbf{r}_i)e^{-\alpha\delta z(\mathbf{r}_i)}. \qquad (30)$$

Here $\delta z(\mathbf{r}_i)$ is the spatial variation of the tip-to-surface distance in the constant-current scanning mode, and α is a constant determined by the work function. The detailed behavior of $m(\mathbf{r}_i)$ is presently unknown and can at best be assumed to have no or very weak spatial dependence. However, the spatial variation in the tip distance $\delta z(\mathbf{r}_i)$ is known in the form of the surface topography from experiments. The normalization procedure we used in Ref. 9 is precisely to remove this part of the matrix element effect such that the resulting data represent tunneling measurements carried out with the tip-to-surface distance effectively held constant. While it has been common practice to present STM data without such a normalization, in which case the low energy inhomogeneity of the tunneling conductance is not clearly revealed,[10,11] we be-
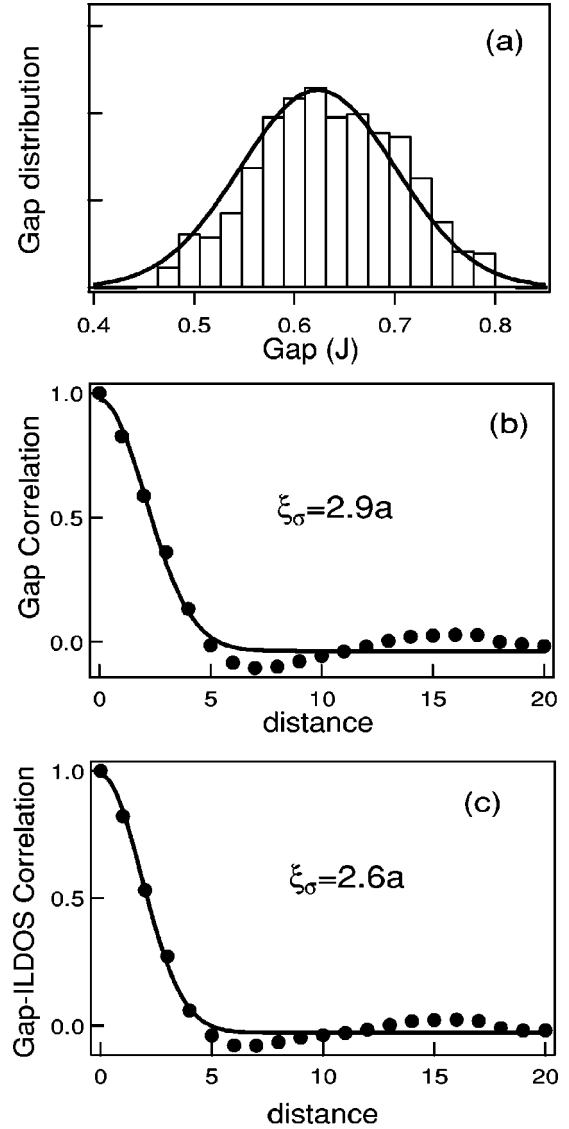

FIG. 12. Statistical properties of the tunneling gap Δ_T. (a) A histogram of Δ_T in the 32×32 system at $x=0.12$, showing approximate Gaussian distribution (solid line). (b) The azimuthally averaged autocorrelation function of the tunneling gap variations. (c) The absolute value of the azimuthally averaged cross-correlation function between the variations in Δ_T and the ILDOS. The solid lines are Gaussian fits.

lieve that the constant tip distance normalization is physical and should be carried out in order to obtain the true electronic contribution to the tunneling spectra. Our theoretical calculations in the inhomogeneous d-wave superconducting state based on *local* spinon pairing and *local* holon condensation indeed support the experimental observation[9] that the low energy STM tunneling spectra is spatially inhomogeneous. We next provide a careful analysis of the theoretical data at zero-bias and make a few predictions that can be tested and used to guide further experiments.

Figure 14(a) shows a 2D map of the zero-bias LDOS at every point on our 32×32 lattice. The spatial variations are obvious, but what is striking is that this is the *same* pattern of inhomogeneity that we saw at the energy scale of the super-
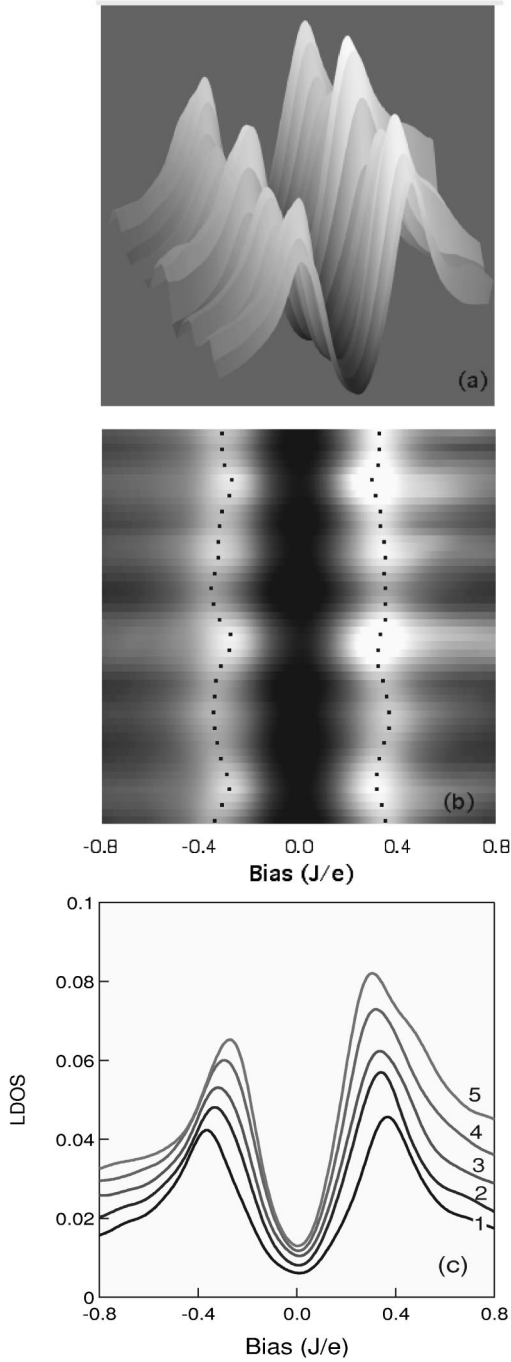
(a)

FIG. 13. Spatial variations of the LDOS spectrum as a function of bias. (a) A three-dimensional rendering of the tunneling spectra along the line-cut indicated in Fig. 10(a). (b) The same data from a bird's-eye view. The black dotted lines trace the locations of the coherence peak. (c) Five characteristic spectra taken at the positions marked in Fig. 10(a). The local doping concentrations are: $x_1 = 0.05$, $x_2 = 0.07$, $x_3 = 0.10$, $x_4 = 0.14$, $x_5 = 0.19$.
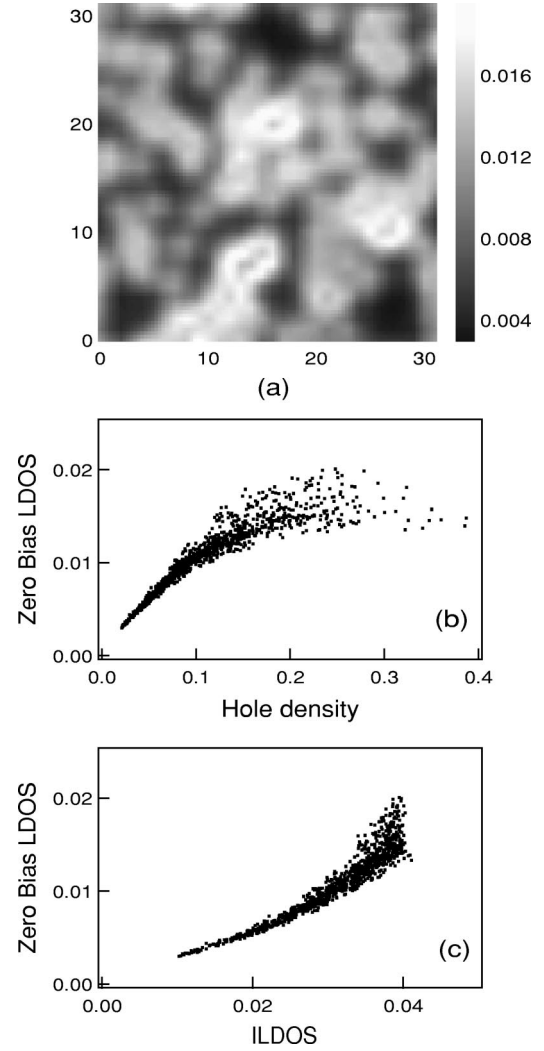

FIG. 14. Spatial inhomogeneity at zero-bias. (a) A 2D map of the zero-bias LDOS, $N_i(0)$, showing the same pattern of inhomogeneity as the tunneling gap map and the ILDOS map in Fig. 10. (b) A scatter plot of $N_i(0)$ versus the LDC x_i. (c) A scatter plot of $N_i(0)$ versus the ILDOS.

troscopy. To further illustrate the correlation between them, we construct a scatter plot of the zero-bias LDOS $N_i(0)$ versus the LDC x_i in Fig. 14(b). It suggests a strong correlation via a linear relationship between the two quantities in the regions of low doping. The scatter increases gradually with increasing LDC and the linear relationship tappers off and saturates. This is quite similar to the behavior of the ILDOS and points to the more intricate x_i-dependence of the LDOS in Eq. (21) beyond the overall linear proportionality.

Since the local doping concentration is not directly accessible experimentally, in Fig. 14(c) we present the scatter plot of the zero-bias LDOS versus the ILDOS. Interestingly, due to the weaker variation of the ILDOS in regions of higher hole concentration [see Fig. 14(b)], the scatter of the zero-bias LDOS exhibits a slight upward curvature with increasing ILDOS. Such a scatter plot can be directly constructed from the STM experimental data for comparison,[36] which serves as another test for the present theory. Two remarks are in order:

conducting gap, as shown in the gap map in Fig. 10(a), in complete agreement with experiments.[36] Moreover, comparing Fig. 14(a) to the local hole density map in Fig. 7(a) shows that they are directly correlated. This strongly suggests that the same kind of inhomogeneity pattern should be observable at *all* energy scales in the STM tunneling spec-
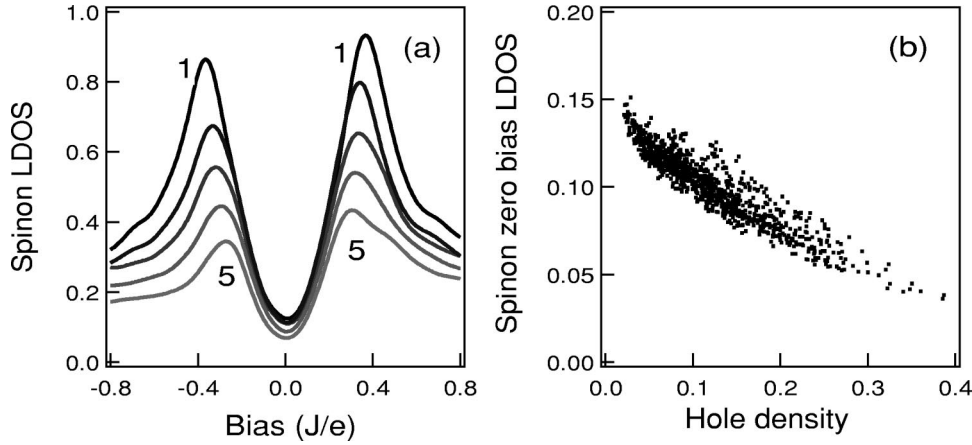
FIG. 15. The tunneling LDOS for spinons. (a) The spinon tunneling spectra at the five positions marked in Fig. 10(a), in comparison to those of the electron tunneling spectra shown in Fig. 13(c) where the LDC x_i, $i = 1, \ldots, 5$ were given. (b) A scatter plot of the spinon zero-bias LDOS versus the LDC x_i, showing remarkable similarity to that of $\Delta_d(i)$ versus x_i presented in Fig. 9(a).

(i) It is important to emphasize the difference between the electron tunneling DOS that spectroscopy measurements probe and the thermodynamic DOS or the compressibility that shows up in thermodynamic measurements such as the specific heat. While the former depends on both the quasi-particle wave function renormalization Z and the self-energy corrections, the latter is insensitive to Z.[21] Although the inhomogeneity in the tunneling spectra at low energies emerges from the spatial variations in the LDC x_i through both the wave function renormalization and the spinon tunneling spectra as described by Eq. (21), its implications on the thermodynamic DOS and the transport properties require a different analysis. We stress that the difference between these two density of states even at our unrestricted mean-field level is more than the local doping concentration x_i, the prefactor in the electron tunneling LDOS, due to the presence of the spinon wave functions in Eq. (21).

(ii) Although the spinon tunneling DOS is not directly accessible by STM measurements, since only the physical electrons can tunnel in and out of the sample, it can be, nevertheless, readily extracted from Eq. (21). Dividing out the prefactor x_i, we show in Fig. 15(a) the spinon tunneling spectra, $N_i^f(\omega) = N_i(\omega)/x_i$, at the five locations marked in Fig. 10(a). Comparing to the corresponding spectral lines for electron LDOS at the same locations shown in Fig. 13(c), it is clear that the degree of inhomogeneity remains large at the energy scale of the superconducting gap. This is not surprising because the gap inhomogeneity results from local spinon pairing in our picture. However, the degree of inhomogeneity appears to have been somewhat reduced at low energies near zero-bias, suggesting that the spinons near the gap nodes, unlike the (electron) nodal quasiparticles, experience less inhomogeneity.[35] The scatter plot of the spinon zero-bias LDOS versus local hole concentration is shown Fig. 15(b). Although the relative magnitude of the variations is reduced by about 30% from the electron case in Fig. 14(a), the spatial variation of the zero-bias conductance for spinons is not only clearly visible, but shows a very well defined correlation with the local hole concentration that is remarkably similar to that of the d-wave order parameter Δ_d shown in Fig. 9(a). Therefore, we conclude that the low energy spinons near the d-wave gap nodes will experience the same type of inhomogeneity as the spinons at the gap edge.

VI. STM TOPOGRAPHY AND THE TUNNELING SPECTRA AT CONSTANT CURRENT

We next derive from our numerical data a theoretical STM topographic image at constant tunneling current for the 32×32 system we study. We then use the result to reconstruct the local tunneling spectra at constant current, which corresponds to the original STM data before normalization. In doing so, we will further illustrate the physics behind the normalization procedure used in Ref. 9, which is essentially a mapping from a constant current topography to the electron LDOS measured at constant tunneling barrier width.

The STM measurements are usually carried out at a constant tunneling current I_0 which is equivalent to the integrated LDOS from the sample bias voltage $-V_0$ to the Fermi level. Thus we can write

$$I_0 = \int_{-V_0}^{0} dV \frac{dI}{dV}[\mathbf{r}, V, z(\mathbf{r})], \tag{31}$$

where $(dI/dV)[\mathbf{r}, V, z(\mathbf{r})]$ is the LDOS or the tunneling differential conductance. It is a function of the 2D coordinates $\mathbf{r}$ on the tunneling surface, the sample bias V, and the tip to surface distance $z(\mathbf{r})$ (topography) that must vary at every $\mathbf{r}$ in order to keep the current I_0 a constant. Note that (dI/dV) in Eq. (31) corresponds precisely to the original STM data before normalization. From our discussion following Eq. (29), it is clear that (dI/dV) is related to the physical electronic tunneling spectra $N(\mathbf{r}, eV)$ obtained at constant $z(\mathbf{r})$ according to

$$N(\mathbf{r}, eV) = \frac{dI}{dV}[\mathbf{r}, V, z(\mathbf{r})]e^{\alpha z(\mathbf{r})}. \tag{32}$$

Integrating Eq. (32) over V from $-V_0$ to 0 gives, after using Eq. (31),

$$I(\mathbf{r}) = I_0 e^{\alpha z(\mathbf{r})}, \tag{33}$$

where $I(\mathbf{r})$ is the electronic ILDOS given by Eq. (27) in terms of the normalized or the calculated tunneling spectra. Equation (33), together with Eq. (32), completely describes the mapping between the constant current topography and the local electron tunneling spectra at constant tunneling barrier width.

From our calculated ILDOS map and using Eq. (33), we obtain the constant current STM topographic image $z(\mathbf{r})$ on our 32×32 lattice using $\alpha = 2.3$ Å^{-1} which corresponds to a work function of about 4 eV. The topography is presented in Fig. 16(a), which exhibits identical structures as the electron ILDOS map shown in Fig. 10(b). We next covert the entire local tunneling spectra $N(\mathbf{r}, V)$ at constant tip-sample distance to the tunneling differential conductance at constant current using Eq. (32) and the topography map. The procedure turns out to be equivalent to normalizing the LDOS spectra by the corresponding ILDOS.

In Fig. 16(b), we show five differential conductance curves at the same five positions marked in Fig. 10(a). Notice that, typical of the raw STM data, the spectral lines on the negative bias side cross approximately at one value of the voltage as a result of the constraint that the integrated area under each curve, i.e., the tunneling current, must be the same. The spatial inhomogeneity on the energy scale of the superconducting gap remains, albeit that the peak height does not show the same systematics—smaller gap with higher coherence peak—as in the experimental data with or without normalization.[36] This discrepancy may be due to the simplification of the mean-field theory which ignores the effects of fluctuations, and perhaps also, to a certain extent, due to the complication of the matrix element effects in the STM tunneling data. The spatial variations of the tunneling differential conductance spectra at low energies are, however, much less visible. The scatter plot of the zero-bias conductance versus local doping concentration is shown in Fig. 16(c). Comparing to the same plot for the electron zero-bias LDOS shown in Fig. 14(b), we find that the relative magnitude of the variations in the zero-bias conductance is suppressed by about 65% and it shows almost no systematic dependence on the LDC. These findings are in good qualitative agreement with the experimental observation that the original STM data before normalization show much less spatial inhomogeneity at low energies.

VII. SUMMARY AND DISCUSSIONS

We have investigated in this paper, through microscopic calculations based on a generalized t-J model, the effects of the off-plane ionic potential associated with off-stoichiometry doping in the *d*-wave superconducting state of a doped Mott-insulator. We find that nonlinear screening dominates the response of the doped Mott-insulator to the ionic potential. One of the main characteristics of nonlinear screening is the emergence of a percolative-type of inhomogeneity in the electronic structure. In 2D electron systems formed in modulation doped semiconductors, nonlinear screening of the ionic dopant potential at low electron densities can tear the 2D electrons into an inhomogeneous mixture of metallic and dielectric regions.[14] What we have shown here is a striking analogy of the physics in a doped Mott-insulator: nonlinear screening of the dopant ionic potential leads to an inhomogeneous *d*-wave superconducting state wherein the LDC and the *d*-wave superconducting gap exhibit significant spatially correlated variations on the scale of a nanometer comparable to the short coherence length. In
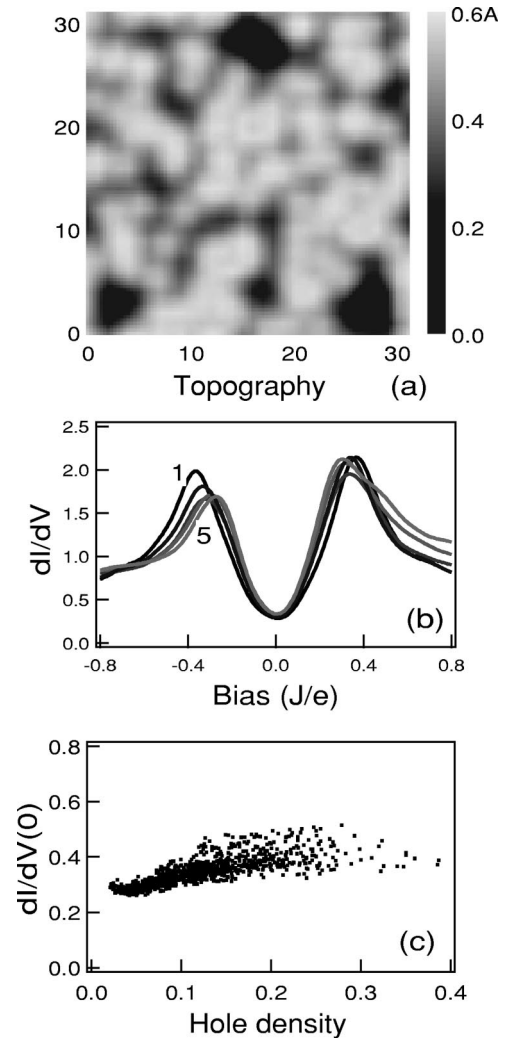

FIG. 16. Calculated STM spectroscopy of the 32×32 lattice in the constant-current mode. (a) The topographic image of our system, showing the same inhomogeneity structures as the electron ILDOS map plotted in Fig. 10(b). (b) The characteristic tunneling differential conductance spectra at the same five positions marked in Fig. 10(a). The integrated area under the spectral lines on the negative bias side is the same, i.e., the constant tunneling current. Note that the inhomogeneous distribution of tunneling differential conductance near zero bias is hardly visible. (c) A scatter plot of the zero-bias conductance versus the LDC.

this context, the concept of a *local doping concentration* augmented by the generalization of the Mott–Hubbard picture to local spectroscopies that we advocate[9] is very useful. We have shown that, within our self-consistent, spatially unrestricted mean-field approach, local spinon pairing and local holon condensation capture the essential physics of the inhomogeneous superconducting state and provide remarkably consistent descriptions of the experimental data.[9]

We have shown that there is one length scale, controlled by the ionic setback distance d_s, that characterizes the inhomogeneity. The decay lengths of the autocorrelations of the spatial variations in the LDC and the *d*-wave pairing order parameter are found to be close to d_s, suggesting that the superconducting pair-size is determined by d_s. In this paper,

we have chosen $d_s = 1.5a$ based on the physical distance of ~ 5 Å between the CuO$_2$ plane and the BiO layer where the dopant oxygen ions reside and $a \simeq 3.8$ Å for the Cu–Cu atomic spacing. However, it is important to emphasize the effects of anisotropy in the background dielectric screening constant which enters the ionic potential. It was pointed out to us by Kivelson that, for the high-T_c cuprates, the background dielectric constant, determined by the electronic interband polarization and phonon contributions, is highly anisotropic, i.e., it has a different value along the c-direction, $\epsilon_\perp$, than in the ab-plane $\epsilon_\parallel$. If this anisotropy is taken into account, the ionic potential given in Eq. (4) must be modified by replacing[37] $V_d \to V_d^*$ and $d_s \to d_s^*$ with $d_s^* = \sqrt{\epsilon_\parallel \epsilon_\perp} d_s$. Thus the *effective* distance between the BiO layer and the CuO$_2$ plane can be significantly larger than 5 Å. Taking $\epsilon_\perp \simeq 8.0$ and $\epsilon_\parallel \simeq 1.5$, it follows that the effective setback distance $d_s^* \simeq 3.5a \simeq 13$ Å. Our results then imply that the pair-size, determined by the decay length in the spatial variation of the d-wave order parameter, would be on the order of one to two nanometers, in good agreement with our experimental findings.[9]

The physics discussed here can be continued to more underdoped cases where the percolative structures resulting from nonlinear screening are expected to be more pronounced. Already in the case of 12% average doping studied here, the tunneling spectra along particular line-cuts in Fig. 10(a) show patches over which the superconducting gap is nearly flat in the center and changes quickly near the edges, indicative of a percolative electronic structure which is often referred to as microscopic phase separation.[6,10,11] As we have shown that the size of the screening cloud around an isolated ion is determined by its effective setback distance d_s^*, it is likely that, with increasing doping, a percolation transition/crossover takes place near optimal doping where the average inter-hole distance becomes comparable to an effective setback distance d_s^*.

We have not discussed the very underdoped physics in detail because in that case it will become important to include the effects associated with magnetism that is not important and has thus been left out in the average doping range considered in this paper. We have tested that if magnetism is included, locally antiferromagnetic ordered insulating regions emerge and percolate at sufficiently low averaged doping. This is left for further studies. Nevertheless, the present theory implies that in underdoped BSCCO, the local tunneling spectra should reveal a percolative structure of superconducting patches embedded in a background where larger tunneling gaps to single-particle excitations arise.

A frequently asked question is how does the high transition temperature coexist with the inhomogeneity. While we do not have a complete answer, we would like to discuss a few relevant issues related to this question. One of the most obvious reasons for high-T_c superconductivity to survive the inhomogeneity is its short coherence length. In our theory, the latter, determined by the effective setback distance d_s^*, is also the scale of the inhomogeneity and will therefore remain shorter than the mean-free path which is usually much larger than the correlation length of the scattering centers for a
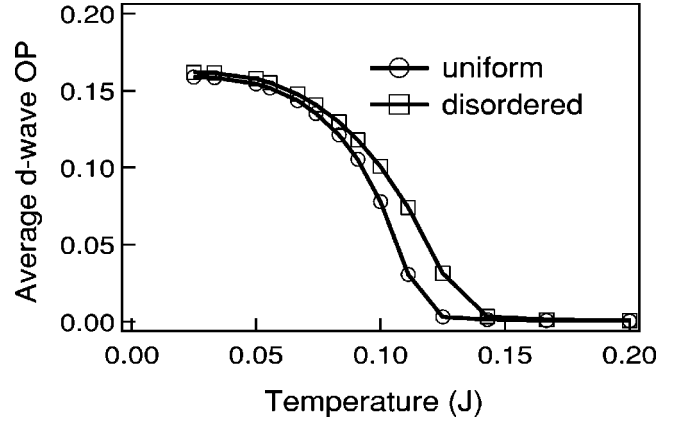

FIG. 17. The temperature dependence of the *averaged* d-wave order parameter (open squares) on a 16×16 lattice at an average doping $x = 0.15$. Also shown in open circles is the temperature dependence of the d-wave order parameter in the uniform d-wave state without the ionic potential.

reasonable scattering strength. Moreover, as we have pointed out in Ref. 9, the scattering by the out-of-plane ionic potential involves predominantly small momentum transfers limited by the small scattering angle on the order of $1/d_s^* k_F$, where k_F is the Fermi momentum. This type of scattering is much less effective at reducing T_c than at increasing the single-particle scattering rate.[38]

We have preliminary results on the temperature dependence of the distribution of the d-wave order parameter Δ_d. In Fig. 17, we plot the *averaged* Δ_d versus temperature on a 16×16 lattice at an average doping $x = 0.15$. Also shown is the temperature dependence of Δ_d in the same system without the ionic potential. Comparing the two curves shows no sign of degradation of T_c defined by the averaged order parameter. Nevertheless, a distribution of Δ_d does imply a distribution of T_c and a finite width of the transition. We leave this topic for future study.

There is no evidence at present that would suggest the inhomogeneity as being necessary for observing high-T_c superconductivity. However, the existence of such inhomogeneity should at least help protect the d-wave superconducting state from other possible competing instabilities. Similarly, from a theoretical perspective, the inhomogeneous d-wave superconducting state with spinon pairing and local holon condensation may do much better at suppressing low-lying fluctuations beyond the self-consistent mean-field solutions than its uniform counterpart.

We next briefly discuss what happens if the dopant ions are more ordered in the BiO layer. Experimentally, thermal annealing is believed to be able to achieve a certain degree of dopant ordering. To this end, we studied a case where the dopant ions are periodically ordered and the average doping $x = 0.14$. We found that the LDC and the d-wave order parameter show spatial variations that are periodic with the same periodicity as that of the dopant ions. The widths of the distribution functions are significantly reduced when compared to the disordered case. We therefore expect that, although the spatial inhomogeneity would remain after thermal annealing, the spatial variations would be more periodic in

structure with a noticeably smaller magnitude.

Based on these results, we expect that the microscopic variations in the electronic properties of YBCO, particularly in its ortho-phase,[2] should be more periodic in space because the oxygen dopants can be ordered in the copper-oxygen chains. However, there exists an important difference in the role of the dopant ions. In BSCCO, the BiO plane is essentially insulating which allows us to treat the dopants as solely providing the dielectrically screened ionic potential. The situation can be very different in YBCO because the chains themselves are conducting and have low energy dynamics of their own. The electrons in the chains will scatter off the dopant ions giving rise to charge density oscillations along the chains that may complicate the way by which carriers are doped into the CuO_2 plane. The present theory would predict the appearance of inhomogeneous electronic structures in the CuO_2 planes of YBCO that are most pronounced directly under/above the doped chains. This type of spatial inhomogeneity on YBCO may have been recently observed.[39]

We have investigated here one of the most direct consequences of off-stoichiometry doping of a Mott-insulator, namely the ionic potential. There are potentially others. For example, the presence of dopants can affect the transfer integrals in their vicinity, causing spatial variations in the parameters t and J, and perhaps more importantly in $t_\perp$ along the *c*-axis. It is therefore plausible that certain aspects of the inhomogeneous superconducting state could also arise from inhomogeneous pairing interactions[40,41] or impurities and defects in the superconducting plane[42,43] and many other kinds studied previously in the context of disordered superconductors. These are interesting and important issues that need to be further investigated.

[1] P. W. Anderson, Science **235**, 1196 (1987).

[2] R. X. Liang, D. A. Bonn, and W. H. Hardy, Physica C **336**, 56 (2000).

[3] H. F. Fong *et al.*, Nature (London) **398**, 588 (1999).

[4] H. Hasegawa *et al.*, in *Physical Properties of High Temperature Superconductors III*, edited by D. M. Ginsberg (World Scientific, Singapore, 1992).

[5] E. L. Wolf *et al.*, J. Supercond. **70**, 355 (1994).

[6] V. J. Emery and S. A. Kivelson, Physica C **209**, 597 (1993); S. A. Kivelson and V. J. Emery, in *Strongly Correlated Electronic Materials*, edited by K. S. Bedell *et al.* (Addison-Wesley, New York, 1994).

[7] Y. Zhang *et al.*, Phys. Rev. Lett. **86**, 890 (2001). Recent measurements on BSCCO by the same group show a 400 Å mean-free-path.

[8] T. Valla *et al.*, Science **285**, 2110 (1999); A. Kaminski, *et al.*, Phys. Rev. Lett. **84**, 1788 (2000); P. V. Bogdanov *et al.*, *ibid.* **85**, 2581 (2000).

[9] S. H. Pan *et al.*, Nature (London) **413**, 282 (2001).

[10] C. Howald, P. Fournier, and A. Kapitulnik, Phys. Rev. B **64**, 100504 (2001).

[11] K. Lang *et al.*, Bull. Am. Phys. Soc. **46**, 804 (2001).

[12] Ch. Renner *et al.*, Phys. Rev. Lett. **80**, 149 (1998); N. Miyakawa *et al.*, *ibid.* **83**, 1018 (1999).

[13] H. Ding *et al.*, Phys. Rev. Lett. **87**, 227001 (2001).

[14] A. L. Efros, Solid State Commun. **65**, 1281 (1988); A. L. Efros, F. G. Pikus, and V. G. Burnett, Phys. Rev. B **47**, 2233 (1993); B. I. Shklovskii and A. L. Efros, *Electronic Properties of Doped Semiconductors* (Springer-Verlag, New York, 1984).

[15] M. S. Hybertsen *et al.*, Phys. Rev. B **45**, 10032 (1992).

[16] J. H. Han, Q.-H. Wang, and D.-H. Lee, cond-mat/0006046 (unpublished).

[17] We find that in the presence of the dopant ionic potential, the tendency toward phase separation is suppressed even without the long-range Coulomb interaction in the doping range of interest here.

[18] G. Baskaran, Z. Zou, and P. W. Anderson, Solid State Commun. **63**, 973 (1987); G. Kotliar and J. Liu, Phys. Rev. B **38**, 5142 (1988).

[19] M. U. Ubbens and P. A. Lee, Phys. Rev. B **46**, 8434 (1992).

[20] Z. Wang, Y. Bang, and G. Kotliar, Phys. Rev. Lett. **67**, 2733 (1991); Z. Wang, Int. J. Mod. Phys. B **6**, 603 (1992).

[21] E. Abrahams, P. W. Anderson, P. A. Lee, and T. V. Ramakrishnan, Phys. Rev. B **24**, 6783 (1981).

[22] D. L. Feng *et al.*, Science **289**, 277 (2000).

[23] H. Tanaka, K. Kuboki, and M. Sigrist, Int. J. Mod. Phys. B **12**, 2447 (1998).

[24] H. Tsuchiura, Y. Tanaka, M. Ogata, and S. Kashiwaya, J. Phys. Soc. Jpn. **68**, 2510 (1999); H. Tsuchiura, Y. Tanaka, M. Ogata, and S. Kashiwaya, Phys. Rev. Lett. **84**, 3165 (2000).

[25] J.-X. Zhu, T. K. Lee, C. S. Ting, and C.-R. Hu, Phys. Rev. B **61**, 8667 (2000).

[26] T. Ando, A. B. Fowler, and F. Stern, Rev. Mod. Phys. **54**, 437 (1982).

[27] T. Deruelle *et al.*, Phys. Rev. B **45**, 9082 (1992).

[28] A. V. Balatsky and M. I. Salkola, Phys. Rev. Lett. **76**, 2386

(1996); A. V. Balatsky, M. I. Salkola, and A. Rosengren, Phys. Rev. B **51**, 15 547 (1995).

[29] M. Franz, C. Kallin, and A. J. Berlinsky, Phys. Rev. B **54**, R6897 (1996).

[30] A. J. Berlinsky *et al.*, Phys. Rev. Lett. **75**, 2200 (1995).

[31] D. Rokshar and S. Kivelson, Phys. Rev. Lett. **61**, 2376 (1988).

[32] Y. Wang and A. H. MacDonald, Phys. Rev. B **52**, R3876 (1995).

[33] A. Ino *et al.*, Phys. Rev. Lett. **81**, 2124 (1998).

[34] We note that in Fig. 3 of Ref. 9, the two tunneling spectra taken at locations where the ILDOS is very small do not show the coherence peaks and the superconducting gaps are absent indicative of insulating behavior. The tunneling spectra in these rare insulating regimes cannot be described by our present mean-field theory which does not include the incoherent contributions that dominates the insulating behavior.

[35] Q.-H. Wang, J. H. Han, and D.-H. Lee, cond-mat/0106038 (unpublished).

[36] S. H. Pan *et al.* (unpublished).

[37] S. A. Kivelson (private communication).

[38] Hae-Young Kee, Phys. Rev. B **64**, 012506 (2001).

[39] A. de Lozanne *et al.* (unpublished); (private communication).

[40] A. I. Larkin and Yu. N. Ovchinnikov, Sov. Phys. JETP **34**, 1144 (1972); L. B. Ioffe and A. I. Larkin, *ibid.* **54**, 378 (1981).

[41] J. S. Meyer and B. D. Simons, Phys. Rev. B **64**, 134516 (2001).

[42] W. A. Atkinson, P. J. Hirschfeld, and A. H. MacDonald, Phys. Rev. Lett. **85**, 3922 (2000).

[43] A. Ghosal, M. Randeria, and N. Trivedi, Phys. Rev. B **65**, 014501 (2002).